Composite Structures 176 (2017) 516–525

Contents lists available at ScienceDirect

Composite Structures

journal homepage: www.elsevier.com/locate/compstruct

Damage resistance of a co-cured composite wing box to low-velocity impact

Zhefeng Yu *, Jicheng Fang, Yan Chen, Hai Wang

School of Aeronautics and Astronautics, Shanghai Jiao Tong University, No. 800, Dongchuan Road, Shanghai 200240, China

ARTICLE INFO

Article history:
Received 15 January 2017
Revised 4 May 2017
Accepted 15 May 2017
Available online 18 May 2017

Keywords:
Wing box
Low-velocity impact
Delamination threshold load
Propagation

ABSTRACT

In this study, low-velocity impacts were applied to an aircraft wing box fabricated by co-curing its spar and skin. The impact points were located at the bay (type A), the T joint (type B), and the spar (type C). The contact force and the energy absorbed by the wing box were compared with those of a full-scale horizontal tail. The contact force of the latter was lower while the energy absorbed was greater. An analytical model is proposed to predict the delamination threshold load of type-B impact based on that of type A, which is effective for both the wing box and the horizontal tail. The static bending test was performed on another wing box after being impacted with 60 J of energy at five locations. The strain responses around the impact point show the propagation of the delamination at the type-A point. The fracture occurred at the location near the fixture rather than at the type-A point. Therefore, the correct impact point should be located on the fracture line in order to investigate the influence of the impact damage on the residual strength of the wing box.

© 2017 Elsevier Ltd. All rights reserved.

1. Introduction

Fibre-reinforced composites are widely used in aircraft structures, such as the control surface, the tail, and even the wing. A well-known problem of composite laminates is their poor resistance to low-velocity impact mainly caused by dropping tools. Delamination is a serious damage because it is generally hard to detect through visual inspection but often induces earlier buckling failure. The delamination threshold load (DTL), energy absorbed, and permanent indentation are the primary parameters for the damage resistance of composite laminates to low-velocity impact [1].

The DTL is the value in the load-time history where a sharp drop occurs as a result of the loss of flexural rigidity due to the occurrence of significant damage, which mainly includes the unstable propagation of delamination [2]. One such analytical model of the DTL is based on fracture mechanics and is given as follows [3–7]:

$$P_{cr} = \frac{2\pi}{3}\sqrt{\frac{2Eh^3G_{II}}{(1-\mu^2)}} \tag{1}$$

where G_{II} is the energy release rate for mode II shear fracture, h is the thickness of the laminate, E is the mean flexural modulus of the laminate in the 0° and 90° directions for the quasi-isotropic lay-up, and μ is the Poisson ratio. Eq. (1) shows that the DTL is proportional to the 3/2 power of the thickness of the laminate. There exists another model, which is based on the interlaminar shear strength and includes the radius of the impactor [8,9]:

$$P_{cr} = \sqrt{\frac{6S_{inter}^3\pi^3h^3R}{E}} \tag{2}$$

where S_{inter} is the interlaminar shear strength, and R is the radius of the impactor tup. Eq. (2) is derived from the shearing stress on the perimeter of the contact region determined using the Hertz contact law [10–12]. In addition, the critical load in Eq. (2) is proportional to $h^{3/2}$ for a certain impactor. This model can be improved by also considering the effect of plate deflection on the contact region [13].

The impact response of an infinite plate is governed by the flexural wave, and the maximum contact force and plate response are not in phase [14]. However, the impact on a small specimen caused by the dropping weight could be regarded as the quasi-static procedure, in which the contact force and plate response are in phase. The spring-mass model is accurate enough for simulating this type of impact [15]. The calculation of the spring stiffness can be found in the studies of Shivakumar et al. [16] and Olsson [17]. This model can also be used to simulate an impact on the skin of a wing box [18]; the spring stiffness is dependent on the length of the wing box and distance between the two adjacent wing spars. However, it is necessary to study the impact on the full-scale wing panel to reveal the characteristics of the impact in different regions.

* Corresponding author.
E-mail address: yuzf@sjtu.edu.cn (Z. Yu).

http://dx.doi.org/10.1016/j.compstruct.2017.05.042
0263-8223/© 2017 Elsevier Ltd. All rights reserved.

Riccio et al. [19] investigated the damage resistance to an impact in a stiffened composite panel under a static load using the finite element (FE) method. The critical impact force is adopted to indicate the onset of the delamination. They then conducted a numerical analysis on the damage behaviour of a localised area in a composite wing box by using the global–local approach [20]. The size of the delamination area obtained from the simulation confirms that obtained through the experimentation. Faggiani et al. [21] simulated a low-velocity impact on a stiffened panel using the FE model. The impact point was located in the middle of the adjacent stiffeners. The simulation of the delamination, contact force, and energy absorption is in good agreement with the experimental data presented in Refs. [22] and [23].

The impact damage at the T-joint of the panel is a particular issue for composite panels. Gorfain et al. [24] simulated the damage in a rib-stiffened panel subjected to ballistic impact by using numerical models; the mode and the extent of damage in the flat panel and the T-joint were predicted. Feng et al. [25] studied the effect of impact damage locations on the buckling and post-buckling behaviours of a stiffened composite. The failure modes include the debonding of the skin from stiffeners, the breaking of the stiffeners, and the tearing and splitting of skin. The edge impact is also an issue that tends to cause larger delamination and intra-ply matrix cracks. The 'discrete ply model' is effective in simulating complex damage due to edge impact [26,27]. The impact damage in the deltoid of the T-joint is a newly discovered issue for a structure with functional composite materials [28,29].

The impact tests could also be conducted on full-scale structures. Lovejoy et al. [30] studied the method for generating barely visible impact damage (BVID) on a stitched composite box associated with a hybrid wing body aircraft. Two types of devices were used to produce the impact damage on the interior, vertical, and under surfaces. Jegley et al. [31] first conducted static tests on the pristine composite box and then conducted test on the damaged one. The effect of damage on the structural response was investigated. Clarke et al. [32] conducted impact tests on a preloaded wing box, which included impacts at the bay, on the spar foot, and on the web. A comparison was made between the structural responses of the impact on the plain laminate and an equivalent impact on the wing box. The peak force is higher and the time duration is shorter for the former than for the latter.

The authors have conducted low-velocity impact tests on a composite horizontal tail supported at its centre [13]. In this work, a composite wing box clamped at two ends is used to characterise the impact responses, which are compared with those of the horizontal tail. A model is established to demonstrate the relationship between the DTLs of the T-joint and the skin. The static test with a bending load is performed on another wing box impacted at five typical points, and the effect of the impact damage on the destruction of the wing box is presented.

2. Composite wing boxes and experiment setup

Two wing boxes fabricated using carbon fibre-reinforced plastic composites are considered in this work: one wing box was used to investigate the responses of the panel to low-velocity impacts, and the other was tested with the static bending load after being impacted at five typical points to demonstrate the influence of the impact damage on the structural strength.

The configuration of the wing box and the test fixture are shown in Fig. 1. The wing box comprises skins and spars. Each spar consists of two beams with a channel cross-section. The deltoid region, i.e. the redundant space formed by the two beams and the skin was filled with the fibre bundle. The skin consists of the stacking sequence of $[45/\text{-}45/0_2/(45/\text{-}45)_2 90]_s$, where direction 1 is along the spar. The thickness of the skin, denoted by t, is 3.76 mm. The skin and the spar were co-cured. The thickness at the T-joint of the flange and the skin, t_1, equals 6.03 mm. Three types of sites on the surface of the wing box were subjected to the low-velocity impact: type A is located at the bay between the spars, type B at the edge of the flange, and type C exactly over the web.

In order to conduct the static test, the wing box was connected to two steel boxes—one for the experimental loading and the other for fixing. A photograph of the static test is shown in Fig. 2. Four hydraulic actuators worked synergistically to exert the torsion and bending on the wing box. The wing box used to investigate the responses to low-velocity impacts was also fixed at its two ends.

A drop tower that could be placed on the wing box was used to produce the low-velocity impact. The configuration of the impactor is also shown in Fig. 2. The tup, which has a diameter of 16 mm, is used for the test on the wing box. The optical fibre sensor was mounted at the bottom of the drop tower to measure the impact velocity along with the velocity measurement grid attached to the impactor. The contact force was measured with the dynamic force sensor PCB 208C05. The mass of the impactor can be adjusted by adding weights. In this study, impacts of energy greater than 65 J were conducted with an impactor of 10.4 kg, while other impacts were conducted with an impactor of 5.3 kg.

The wing box is a typical part of a composite horizontal tail. The authors also conducted impact tests on the horizontal tail. The schematic of the fixtures setup and regions of the skin are shown in Fig. 3. The experimental data of type-A impact were used to demonstrate the improved DTL model proposed by the authors [13]. The impacts of type B and type C were also applied to the horizontal tail. The regions of skin are variant in layup and thickness, some of which are listed in Table 1 where the parameters of region 2 are the same as those of the above wing box.

The time history of the energy absorbed by the structure was computed with the kinetic energy and gravitational energy of the impactor. The acceleration of the impactor was computed with the contact force and the mass of the impactor, and the velocity and displacement of the impactor were then obtained by integrating the acceleration and velocity over the impact period, respectively. The energy absorbed by the structure is given as follows [1]:

$$E_a(t) = \frac{m(v_0^2 - v(t)^2)}{2} + mgx(t) \tag{3}$$

where v_0 is the impact velocity, m is the mass of the impactor, g is the acceleration due to gravity, and $v(t)$ and $x(t)$ denote the velocity and displacement at time t, respectively.

3. Results of impact tests

3.1. Impact of type A

Impact tests with energy ranging from 10 J to 60 J were conducted on the type-A position of the wing box. The curve of the contact force versus time is shown in Fig. 4. To investigate the indentation, an impact of 55 J was also applied, the force curve of which is similar to that of an impact of 60 J but is not shown in Fig. 4. The dimensions of the damage area were obtained using ultrasonic C-scans as listed in Table 2, and the image for the impact of 40 J can be found in Fig. 5. There is a sharp drop in each curve for the impact greater than 10 J, and therefore, the corresponding DTL is determined as listed in Table 3, which yields an average of 5802 N. There is no sharp drop in the curve of the 10-J impact, no damage was detected for this impact, and its peak force is lower than the DTL of the 15-J impact, i.e. 5290 N. For damage-resistant design considerations, a designer may predict the impact force of

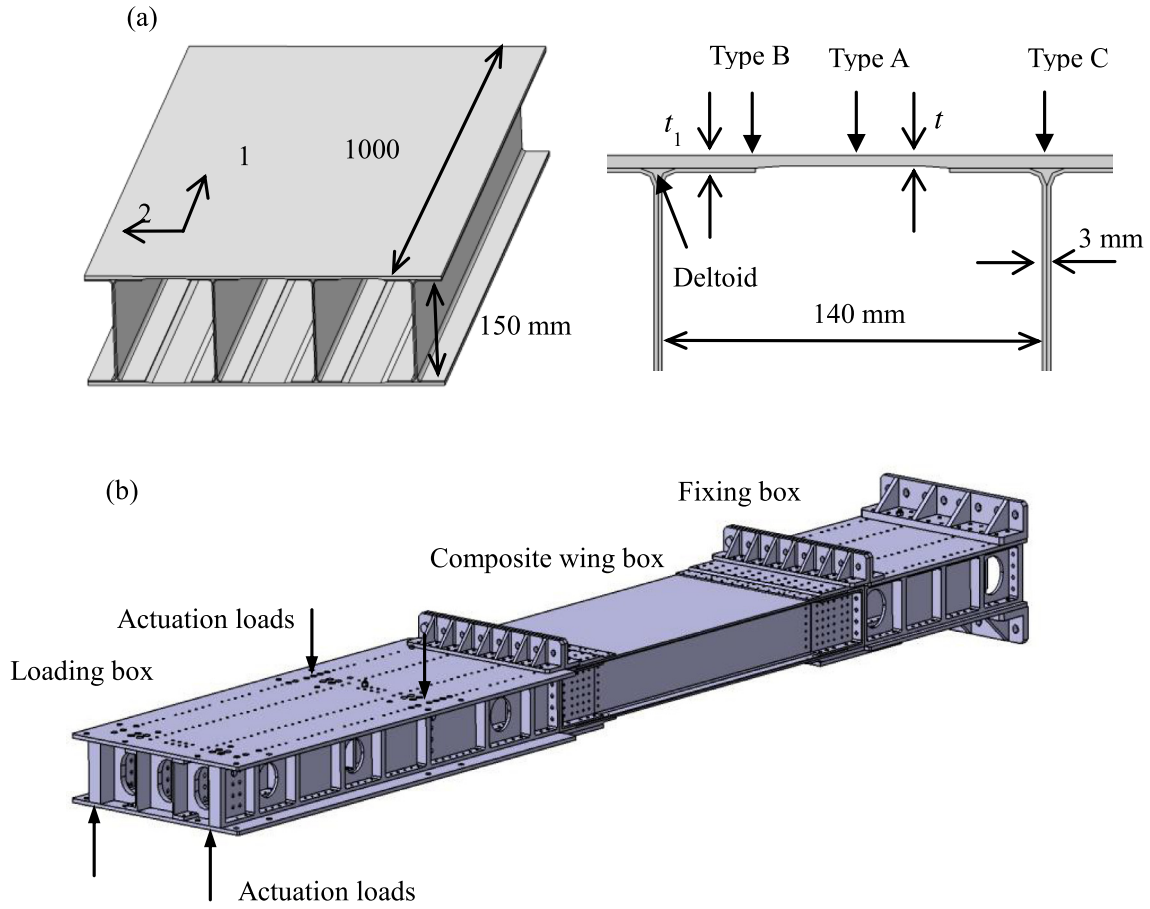

Fig. 1. Wing box structure: (a) details of the wing box and (b) global view with the fixtures.

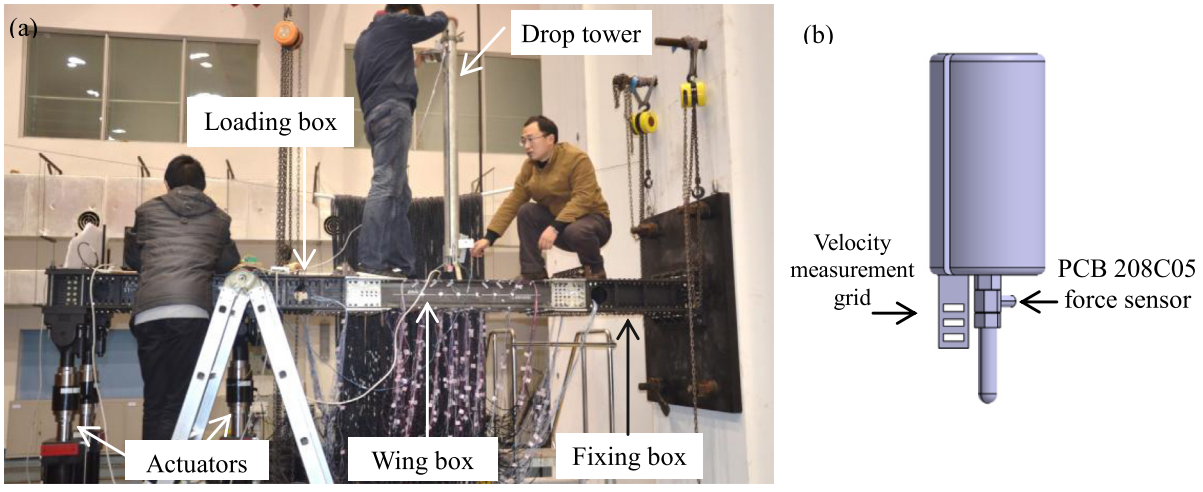

Fig. 2. Experiment setup for static test and impact test: (a) fixtures and test article and (b) components of the impactor.

the undamaged structure. If the predicted peak force is less than 5290 N, then the structure does not incur significant damage. The impact of type A is equivalent to that on a rectangular plate. Consequently, the time history of the contact force is similar to the half-sinusoidal wave in the range from 0 to π according to the spring-mass model without the occurrence of damage. The peak force is easy to predict if the response of the entire structure is not considered.

The dramatic load drop at the peak in the 60-J curve was likely caused by the occurrence of a major portion of the delamination damage. The crushing of the matrix and the breakage of the fibre were also generated at the point subjected to the impact of 60 J, and a significant indentation was then observed (Fig. 6 (a)). The extent of damage can be also reflected in the energy absorbed by the structure (Fig. 7). If no damage is generated, most of the energy will be converted into the kinetic energy of the impactor during its rebound. The increase in the damage may release the elastic energy stored in the deformed structure and then weaken the rebound. Hence, the percentage of the absorbed energy of the 60-J impact is the highest. Although no damage was detected for

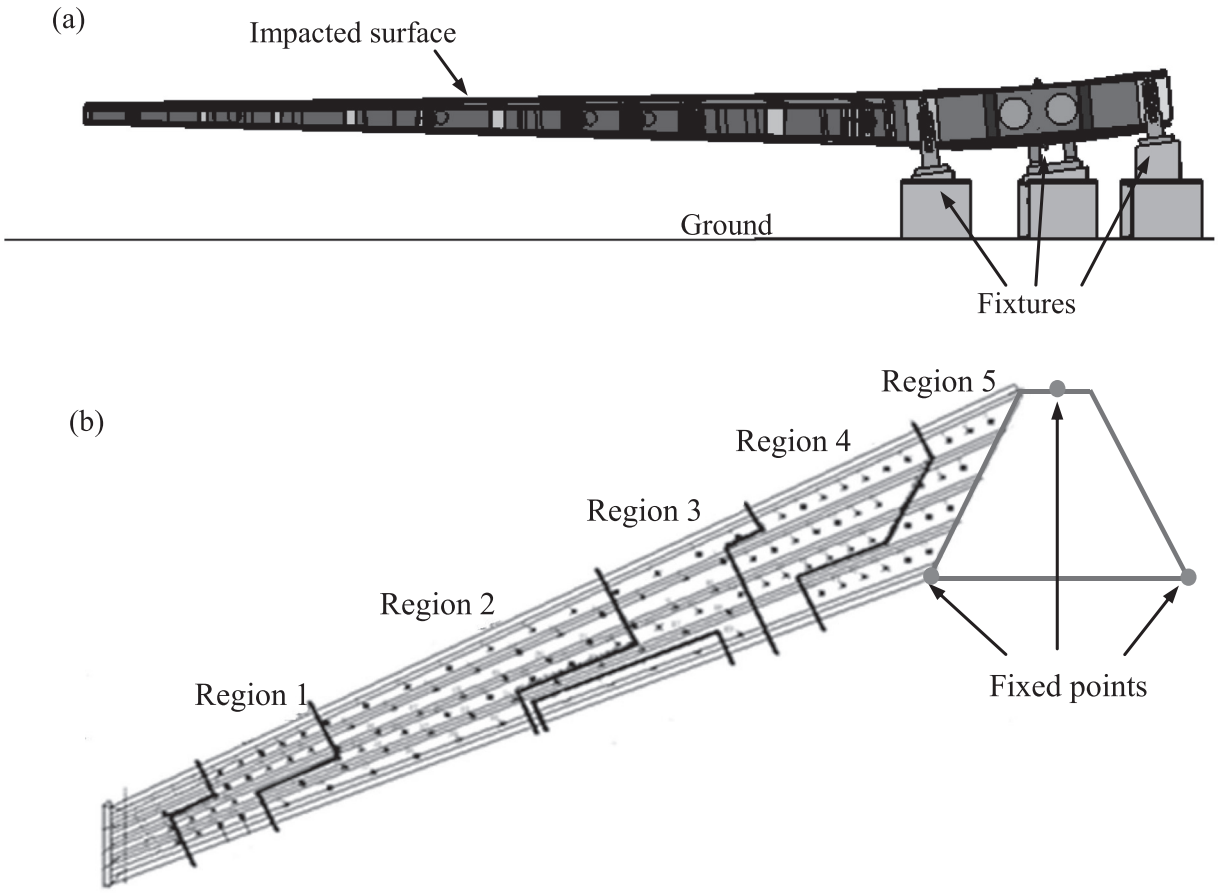

Fig. 3. Composite horizontal tail: (a) fixtures setup in the rear view and (b) regions subjected to impact in the top view.

Table 1
Layup parameters of the regions of the composite horizontal tail.

Regions	Plies amount	t/mm	t_1/mm
Region 2	20	3.76	6.03
Region 3	24	4.51	7.22
Region 5	40	7.52	3.61

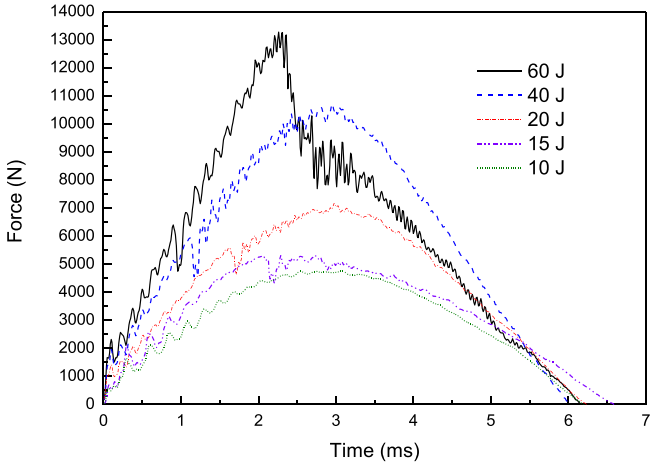

Fig. 4. Contact force histories of the type-A impact on the wing box.

Table 2
Dimensions of the damage area of the wing box.

Impact type	Impact energy (J)	Dimensions of damage area along direction 1 and direction 2 (mm × mm)
A	15	27.8 × 16.5
	20	21.0 × 23.3
	40	38.3 × 27.1
	60	33.8 × 26.3
B	20	45.8 × 23.3
	40	30.8 × 12.8
	65	40.5 × 18.8
C	20	9.0 × 7.5
	40	13.5 × 11.3
	60	15.0 × 19.5

the 10-J impact, the corresponding energy absorption is not equal to zero owing to the damping of the structure.

The contact force curves of regions 2 and 3 of the horizontal tail are shown in Fig. 8, where the responses to the delamination onset are manifested. The dramatic oscillation is presented in the contact force history of region 2 around the peak, showing that serious damage was generated at approximately 9000 N. The time histories of the energy absorption for the horizontal tail are shown in Fig. 9. The energy absorption at the end of the impact is much higher than that of the impacts on the wing box because the energy dissipation in the response of the larger structure is more significant.

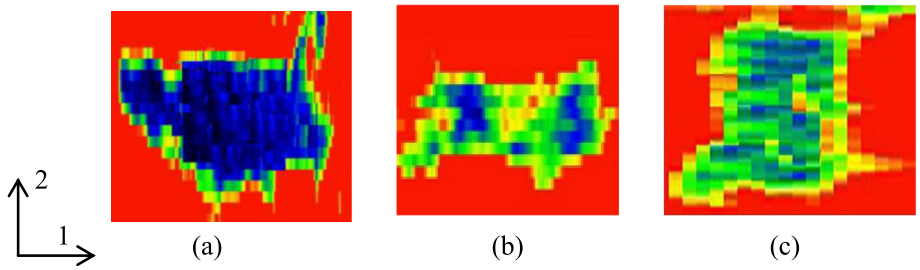

Fig. 5. Ultrasonic C-scans of the delaminations under the 40-J impacts: (a) type A, (b) type B, and (c) type C.

Table 3
DTL prediction for type B for the wing box.

Impact energy (J)	Experimental DTL for type A (N)	Experimental DTL for type B (N)	Predicted DTL for type B (N)	Prediction error/%
65	–	7059	–	–
60	6395	7049	7449	5.7
40	5946	6773	6926	2.3
20	5579	6608	6498	1.7
15	5290	–	6162	–
Average	5802	6872	6758	1.7

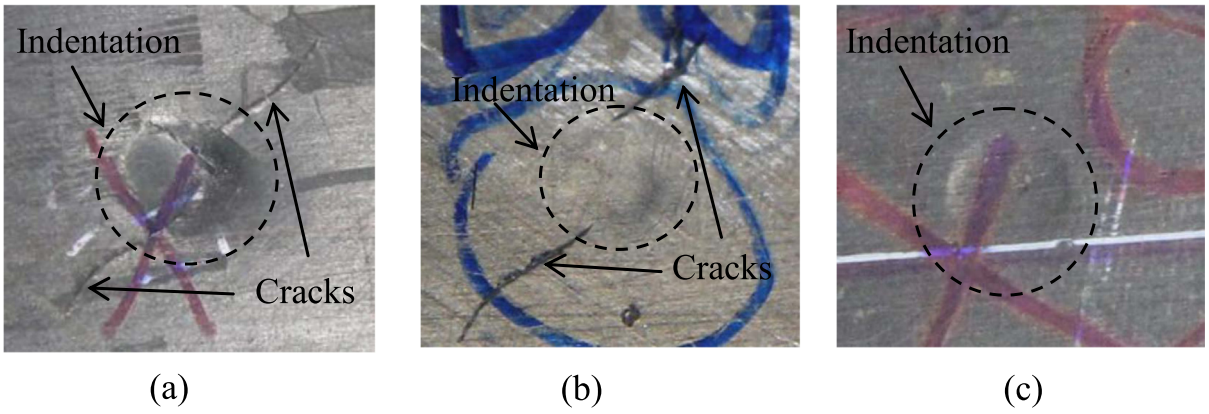

Fig. 6. Photographs of the indentation due to the impact of 60 J: (a) type A, (b) type B, and (c) type C.

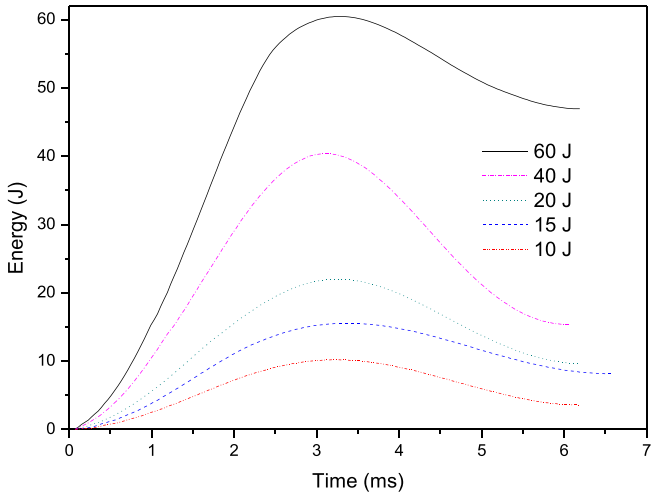

Fig. 7. Time histories of energy absorbed in the type-A impact on the wing box.

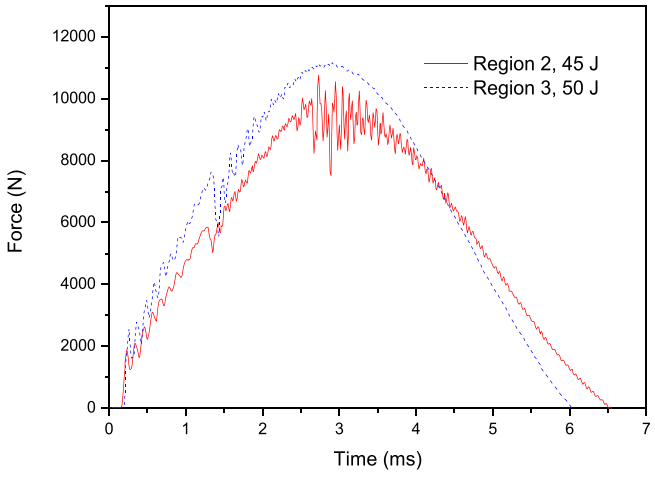

Fig. 8. Contact force histories of the type-A impact on the horizontal tail.

3.2. Impact of type B

Impact tests of energy ranging from 10 J to 65 J were conducted at the type-B position of the wing box. The contact force curves of the type-B impact showed slight asymmetry (Fig. 10). No damage was detected at the point subjected to the 10-J impact, and the C-scans image for the 40-J impact is shown in Fig. 5. A sharp drop also appears in the curves of impact energy greater than 10 J, and the cor-

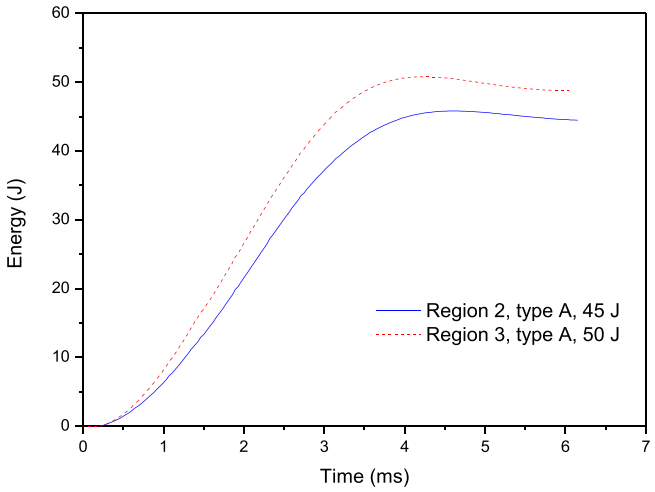

Fig. 9. Time histories of absorbed energy of the type-A impact on the horizontal tail.

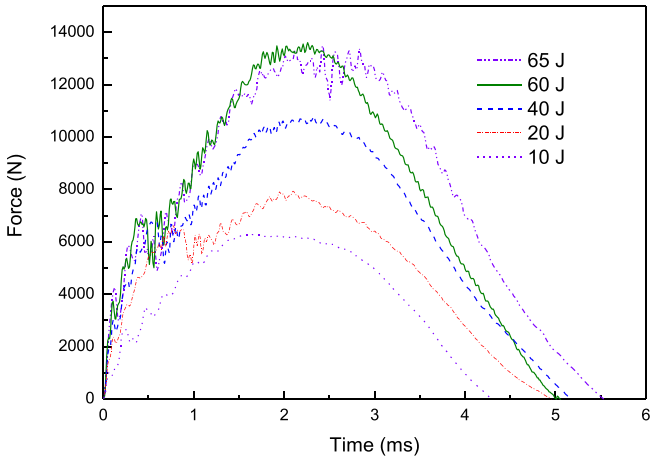

Fig. 10. Contact force histories of the type-B impact on the wing box.

responding DTL is listed in Table 3, where the average DTL is equal to 6872 N. The time histories of the absorbed energy are shown in Fig. 11, where the final absorbed energy of 65 J is the highest.

The contact force curves of the type-B impact of the horizontal tail are shown in Fig. 12. The 80-J curve has a different shape. Three

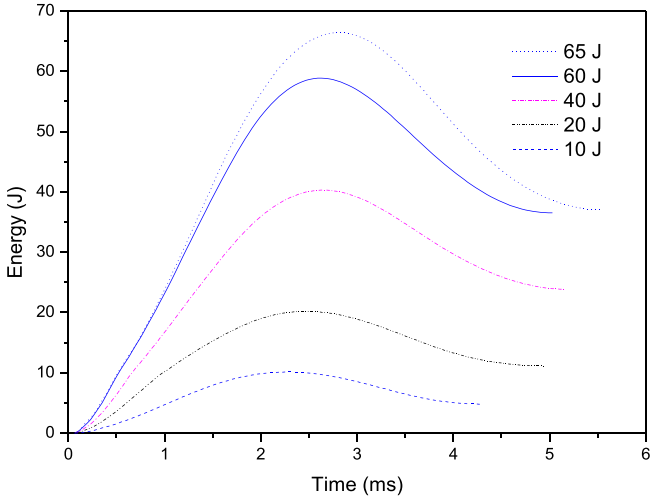

Fig. 11. Time histories of absorbed energy of the type-B impact on the wing box.

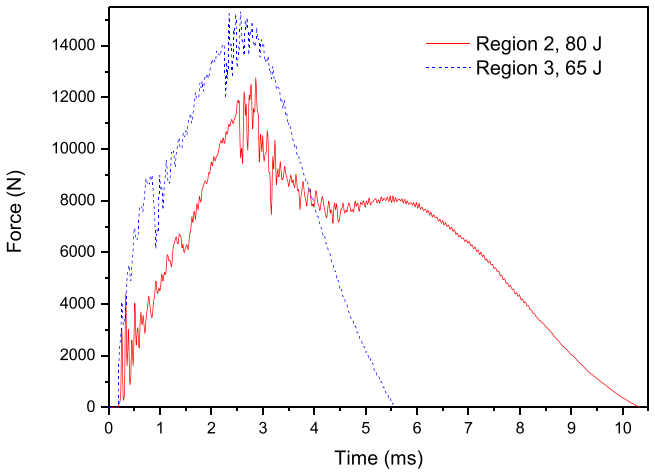

Fig. 12. Contact force histories of the type-B impact on the horizontal tail.

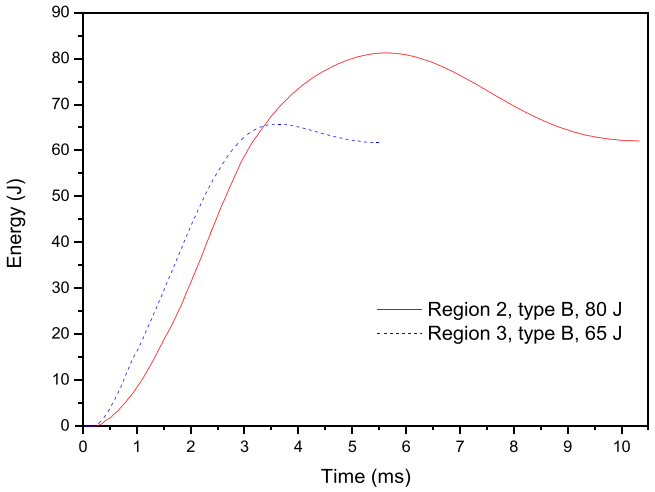

Fig. 13. Time histories of the absorbed energy of the type-B impact on the horizontal tail.

impact tests were conducted at region 2 with an energy of approximately 80 J, and the curves of the contact force were found to be similar. The indentation of region 2 was equal to 2.2 mm, which is associated with the damage that occurs in the fibre and matrix. The time duration of the impact at region 2 was longer because the displacement of the impactor was greater owing to the indentation and the deflection in the horizontal tail. Therefore, the special shape of the contact-force curve indicates the serious damage and reflects the global responses of the horizontal tail. The time histories of the energy absorption are shown in Fig. 13, where the percentage of energy finally absorbed by the horizontal tail is also greater than that absorbed by the wing box.

3.3. Impact of type C

Impact tests of energy ranging from 10 J to 60 J were conducted on the type-C position to obtain the time histories of the contact force as shown in Fig. 14. The time duration of this type of impact is much shorter than that of other two types because of the support of the wing spar. There is a secondary bump after the peak in the 40-J and 60-J load curves. The curves of the impactor displacement are used to analyse this phenomenon, as shown in Fig. 15. The peak displacement of the impactor lags behind that of the contact force, which indicates that the impactor moved further after the peak of the contact force until it reached the extremum. It can be deduced

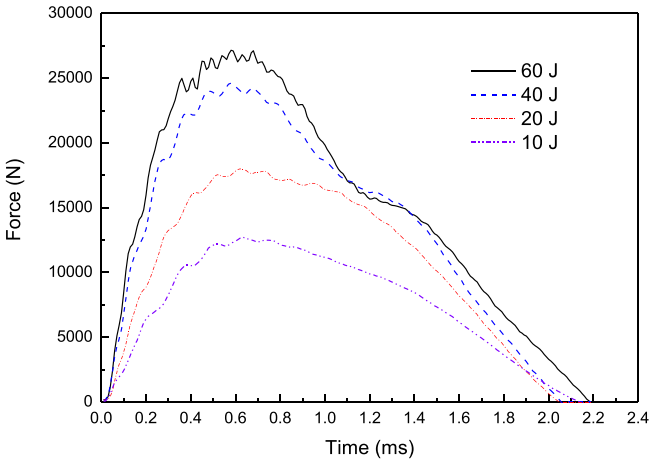

Fig. 14. Contact force histories of the type-C impact on the wing box.

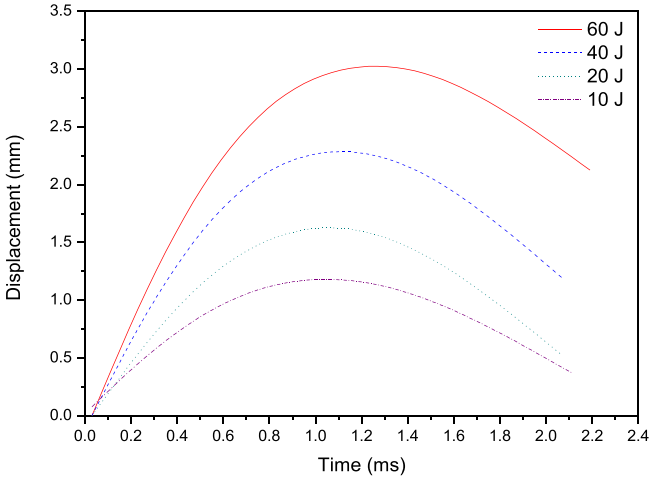

Fig. 15. Displacement histories of impactor in the type-C impact on the wing box.

that the web of the wing spar dominated the peak force in the early stage of contact, and its supporting stiffness then became weak owing to its deflection. It was the change in the structural stiffness that allowed the impactor to move further rather than to rebound. The basic vibrational frequency of the web is 390 Hz according to the vibration theory of a plate. The time interval between the peak of the contact force and that of the impactor displacement was 0.7 ms, which is shorter than the half period of the vibration of 390 Hz. This indicates that the web would not recover at the onset of the peak displacement of the impactor once it is deformed under the impact.

No sharp drop occurs in the contact force history of the type-C impact to indicate the value of the DTL. However, damage was detected at the points at which an impact of energy ranging from 20 J to 60 J was applied, as listed in Table 2. The C-scans of the 40-J impact point are also shown in Fig. 5. The energy absorption shown in Fig. 16 is greater than most impacts of type A and type C although no significant damage was caused; therefore, it is expected that the response of the web had dissipated most of the energy.

The load curves of the type-C impact in regions 2 and 3 of the horizontal tail are shown in Fig. 17, where the peak values are much lower than that of the wing box. A sharp drop is observed in the curve, and the corresponding DTL is much greater than that of the impacts at type-A and type-B positions. The type-C point was not precisely located near to the wing spar of the horizontal tail, and thus, the impact was more likely to occur on the flange.

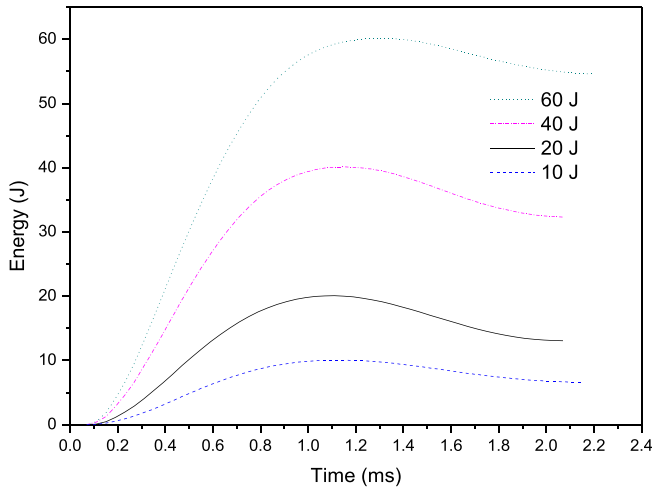

Fig. 16. Time histories of absorbed energy of the type-C impact on the wing box.

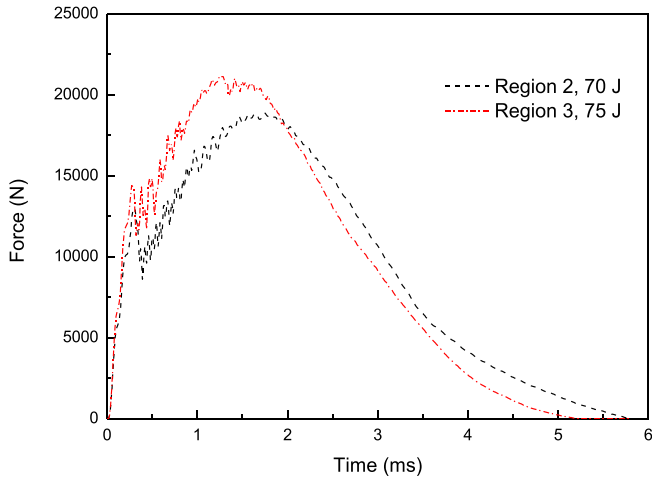

Fig. 17. Contact force of the type-C impact on the horizontal tail.

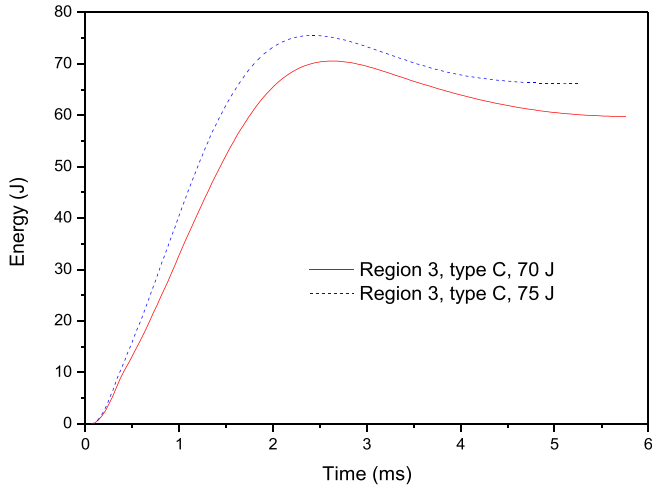

Fig. 18. Energy absorption of the type-C impact on the horizontal tail.

This factor produced the difference in the results of the horizontal tail. The time histories of the energy absorbed by the horizontal tail, which is much higher than that of the wing box, are shown in Fig. 18. The horizontal tail with its root fixed has a lower global

stiffness in comparison to the wing box that is fixed at two ends; therefore, most of the impact energy was absorbed owing to the response of the overall structure.

3.4. Prediction of DTL for type-B impact

A method is proposed to predict the DTL of type-B location with the experimentally determined DTL of type-A location. If the DTL of type A is denoted by P_{crA} and that of type B by P_{crB}, then P_{crB} can be written as

$$P_{crB} = P_{crA}[1 + (\frac{t_1 - t}{2t})^{3/2}] \quad (4)$$

where t and t_1 are shown in Fig. 1. Eq. (4) indicates that the increment of the thickness of the laminate at the flange, i.e. $t_1 - t$, enhances the delamination resistance. As only half of the impact site obtains the support of the flange, the total contribution of the flange to the delamination resistance in terms of thickness is equal to $(t_1 - t)/2$. The DTL is proportional to the 3/2 power of the thickness as shown in Eqs. (1) and (2), which indicates that Eq. (4) is reasonable. The type-B DTL was predicted using the type-A DTL which was measured with the same impact energy (Table 3). The predicted result is in good agreement with the experimental data for the same impact energy. The average DTL of type A was also used to predict the type-B DTL, and the deviation between the predicted result and the average of the experimental DTL of type B is only 1.7%. Moreover, it should be noted that the experimental DTL increases with the impact energy, and hence, the prediction accuracy reduces if the energy of the impact deviates from the average excessively.

Eq. (4) was also used to predict the DTL of the horizontal tail. The tup of 16-mm diameter was applied to the regions 2 and 3, and the tup of 12.7-mm and 25.4-mm diameters were applied to region 5. The DTLs of the type-A and type-B impacts of the regions 2 and 3 are shown in Fig. 8 and Fig. 12, respectively. Because no type-A impact was applied at region 5, the DTL of the type-A impact at region 5 was calculated using the experimental DTL of region and Eq. (2). The DTL of the type-B impact predicted using Eq. (4) is in good agreement with the experimental data listed in Table 4.

3.5. The impact indentation

The indentation was measured immediately after each impact test. The curves of the indentation with respect to the impact energy for the wing box are shown in Fig. 19. An indentation of less than 0.2 mm is generally regarded as BVID. The energy of the impact that caused the general visible indentation is 55 J for the type-A impact and 65 J for the type-B impact. The indentation of type B is barely visible under the impact of 60 J; however, cracks are generated on the surface (Fig. 6 (b)). There was almost no indentation for the type-C impact, but a scar due to the high contact force was found (Fig. 6 (c)).

Table 4
DTL prediction of type B for the horizontal tail.

Regions	Tup diameter (mm)	Experimental DTL for type A (N)	Experimental DTL for type B (N)	Predicted DTL for type B (N)	Prediction error/%
Region 2	16	5853	6647	6817	2.5
Region 3	16	7558	8964	8803	1.8
Region 5	12.7	(14498)*	17306	16210	6.8
Region 5	25.4	(20503)*	21427	22924	6.5

* The data in parenthesis was calculated using the experimental DTL of region 3 and Eq. (2).

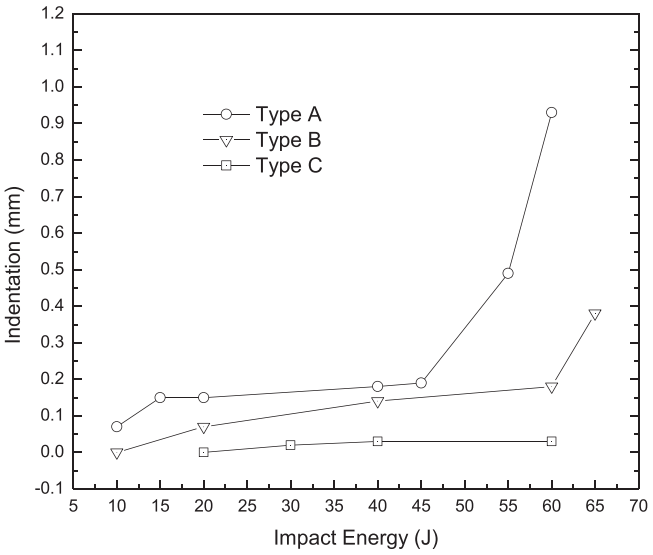

Fig. 19. Comparison of indentations of impacts on the wing box.

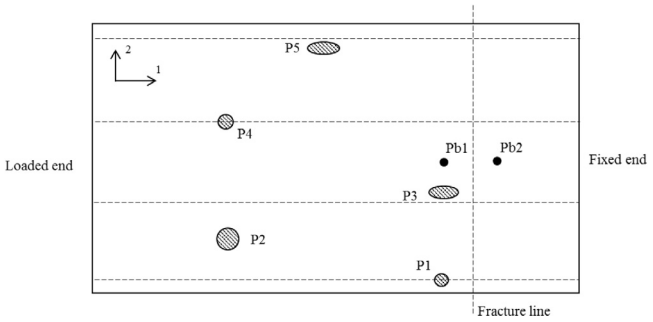

Fig. 20. Impact points and delamination regions of the wing box.

Table 5
Size of delamination area.

Impact point	Impact type	Size of delamination area (mm)
P1	Type C	Φ20
P2	Type A	Φ50
P3	Type B	60 × 45
P4	Type C	Φ40
P5	Type B	75 × 40

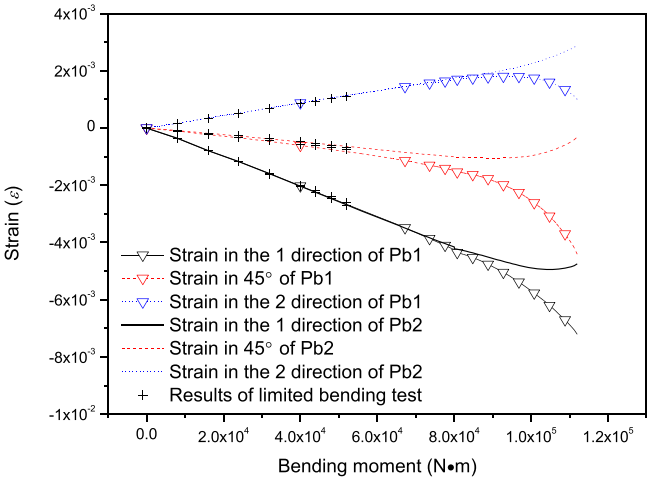

Fig. 21. Strains beside the broken line of the wing box.

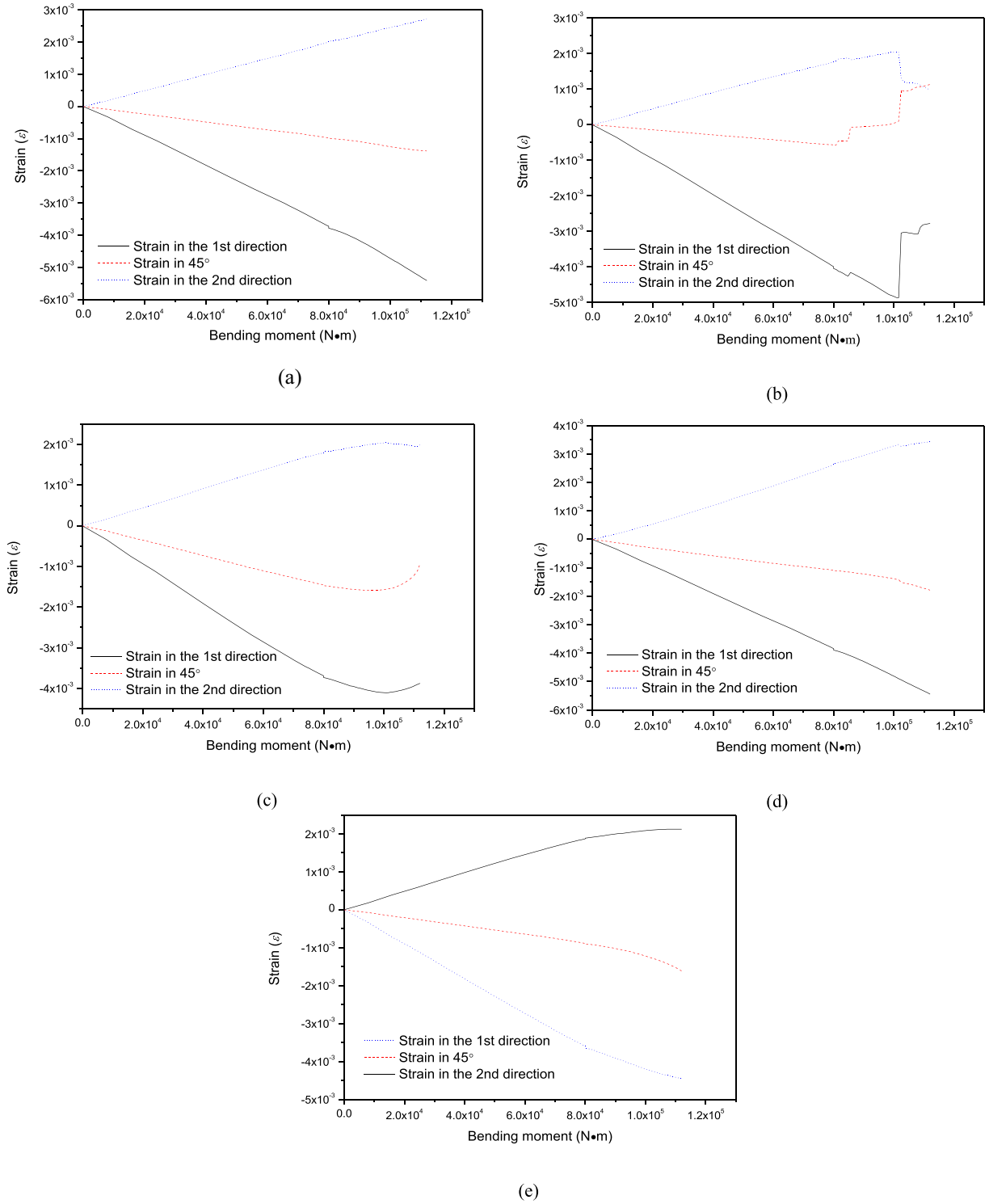

Fig. 22. Strains at the impact points of the wing box: (a) P1, (b) P2, (c) P3, (d) P4, and (e) P5.

4. Ultimate load test after the low-velocity impact

A limited bending moment of 0.5×10^5 N·m was applied to the other wing box without damage first. Five impact tests of 60 J were then conducted on the upper surface of the wing box. Impact points, P1 to P5, are shown in Fig. 20. The sizes of the delamination areas, as listed in Table 5, were detected using ultrasonic scanning. Strain gauges were arranged around the damaged region.

The bending load was again applied to the wing box with impact damage, which was then broken along the line shown in Fig. 20 at the bending moment of 1.1×10^5 N·m. The strains at points Pb1 and Pb2 beside the fracture line were measured with strain rosettes, as shown in Fig. 21. The strains conform to those of the intact structure under the limited load, indicating that the impact damage does not weaken the capability of the wing box to bear the limited load. The critical load of buckling of the wing

box is approximately 0.8×10^5 N·m, after which the strains of the two points divaricated quickly. The divarication of strain also indicates that Pb1 and Pb2 are located at the concave and convex portions of the wave, respectively, during the buckling of the skin.

The strains around the impact points are shown in Fig. 22. The strain at P1 remains linear as the bending load increases. The strain at P2 decreases above 8×10^4 N·m, which indicates the degradation of the load-supporting capability of this region, i.e. the propagation of delamination. A similar observation was made regarding the strain at P4 in the second direction. As a result of being near the wing spar, P3 was located at the convex of the skin during the buckling. Therefore, the amplitude of the strains at P3 decreased before the wing box failed even though P3 was on the same side of the broken line as Pb1. The strains in the first and second direction at P5 were also decreased.

5. Conclusions

The contact force, energy absorption, delamination, and indentation due to a low-velocity impact on the panel of a composite wing box have been investigated in this study. The experimental research involved the use of three types of impact points in a wing box and a horizontal tail.

The characteristics of the type-A impact are consistent with those obtained from the standard test on the specimen. The force–time curves of the type-B and type-C impact exhibit evident asymmetry owing to the effect of the structural components. The sharp drop in the force–time curve, which is associated with the propagation of delamination, is observed for the type-A and type-B impacts that had caused the delamination. Very high contact force is generated by the type-C impact, but the size of the delamination area is small, and a shallow indentation is observed. The energy absorption is high when other parts of the structure are involved in the impact, especially for the impacts on the horizontal tail.

The proposed model is effective in predicting the DTL of the type-B impact with the experimentally determined DTL of type A for the same impact energy. However, it should be noted that the DTL increases slightly with the impact energy, and hence, there will be some deviation if the impact energy of the predicted DTL is different from that of the experimental DTL of the type-A impact.

The wing box with impact damage was used to investigate the behaviour of the damaged region under a compressive load. The wing box was broken owing to the fracture of the panel after it began to buckle. The strain response at the other impact points exhibited good damage resistance to type-B and type C impacts. The failure position is close to the supporting end rather than the impact point where the delamination propagation occurs. Hence, the impact point should be located in this region when investigating the effects of the impact damage on the ultimate load of the composite panel.

Acknowledgment

The author thanks the National Natural Science Foundation of China for the support provided (Grant No. 11372192).

References

[1] ASTM D7136/D7136M-12-Standard test method for measuring the damage resistance of a fiber-reinforced polymer matrix composite to a drop-weight impact even, 2012.
[2] Schoeppner GA, Abrate S. Delamination threshold loads for low velocity impact on composite laminates. Compos A 2000;31:903–15.
[3] Davies GAO, Robinson P. Predicting failure by debonding/delamination, AGARG: 74th Structures & Materials Meeting, Debonding/Delamination of Composites.
[4] Davies GAO, Zhang X. Impact damage prediction in carbon composite structures. Int J Impact Eng 1995;16(1):149–70.
[5] Zhang X. Impact damage in composite aircraft structures—experimental testing and numerical simulation. Proc Inst Mech Eng 1998;212:245–59.
[6] Suemasu H, Majima O. Multiple delaminations and their severity in circular axisymmetric plates subjected to transverse loading. J Compos Mater 1996;30(4):441–53.
[7] Suemasu H, Majima O. Multiple delaminations and their severity in nonlinear circular. J Compos Mater 1998;32(2):123–40.
[8] Sutherland LS, Guedes Soares S. Contact indentation of marine composites. Compos Struct 2005;70(3):287–94.
[9] Yang FJ, Cantwell WJ. Impact damage initiation in composite materials. Compos Sci Technol 2010;70:336–42.
[10] Tan TM, Sun CT. Use of statical indentation laws in the impact analysis of laminated composite plates. Trans ASME 1985;52:6–12.
[11] Wu E, Shyu K. Response of composite laminates to contact loads and relationship to low-velocity impact. J Compos Mater 1993;27(15):1443–64.
[12] Christoforou AP. On the contact of a spherical indenter and a thin composite laminate. Compos Struct 1993;26(1–2):77–82.
[13] Yu Z, Gao S. Increase of contact radius due to deflection in low velocity impact of composite laminates and prediction of delamination threshold load. Compos Struct 2016;147:286–93.
[14] Olsson R. Impact response of orthotropic composite plates predicted from a one-parameter differential equation. AIAA J 1992;30(6):1587–96.
[15] Abrate S. Modeling of impacts on composite structures. Compos Struct 2001;51(2):129–38.
[16] Shivakumar KN, Elber W, Illg W. Prediction of impact force and duration due to low-velocity impact on circular composite laminates. J Appl Mech 1985;52:674–80.
[17] Olsson R. Analytical prediction of large mass impact damage in composite laminates. Compos A 2001;32(9):1207–15.
[18] Yu Z, Yi P, Wang H. Low-velocity impact test of a composite wing box and analytical prediction of contact indentation. 54th AIAA/ASME/ASCE/AHS/ASC Structures, Structural Dynamics, and Materials Conference, April 8-11, 2013, Boston, Massachusetts, USA
[19] Riccio A, Tessitore N. Influence of loading conditions on the impact damage resistance of composite panels. Comput Struct 2005;83(28–30):2306–17.
[20] Riccio A, Ricchiuto R, Damiano M, Scaramuzzino F. A numerical study on the impact behaviour of an All-composite Wing-box. Procedia Eng 2014;88:54–61.
[21] Faggiani A, Falzon BG. Predicting low-velocity impact damage on a stiffened composite panel. Compos A 2010;41(6):737–49.
[22] Greenhalgh E, Meeks C, Clarke A, Thatcher J. The effect of defects on the performance of post-buckled CFRP stringer-stiffened panels. Compos A 2003;34(7):623–33.
[23] Greenhalgh E, Clarke A, Thatcher J. Mechanical evaluation of stringer-stiffened panels tested under compression. Report: DERA.T3.TR.4. Farnborough (UK); 2000.
[24] Gorfain JE, Key CT. Damage prediction of rib-stiffened composite structures subjected to ballistic impact. Int J Impact Eng 2013;57(57):159–72.
[25] Feng Y, Zhang H, Tan X, He Y, An T, Zheng J. Effect of impact damage positions on the buckling and post-buckling behaviors of stiffened composite panel. Compos Struct 2016;155:184–96.
[26] Ostré B, Bouvet C, Minot C, Aboissière J. Finite element analysis of CFRP laminates subjected to compression after edge impact. Compos Struct 2016;153:478–89.
[27] Ostré B, Bouvet C, Minot C, Aboissière J. Experimental analysis of CFRP laminates subjected to compression after edge impact. Compos Struct 2016;152:767–78.
[28] Norris CJ, Bond IP, Trask RS. Healing of low-velocity impact damage in vascularised composites. Compos A 2013;44(1):78–85.
[29] Cullinan JF, Wisnom MR, Bond IP. Damage manipulation and in situ repair of composite t-joints. J Aircraft 2016:1–9.
[30] Lovejoy AE, Przekop A. Imparting barely visible impact damage to a stitched composite large-scale pressure box. 57th AIAA/ASCE/AHS/ASC Structures, Structural Dynamics, and Materials Conference, 4-8 January 2016, San Diego, California, USA.
[31] Jegley DC, Rouse M, Przekop A, Lovejoy AE. Testing of a stitched composite large-scale pressure box. 57th AIAA/ASCE/AHS/ASC Structures, Structural Dynamics, and Materials Conference, 4-8 January 2016, San Diego, California, USA
[32] Clarke A, Greenhalgh E, Millson B, Jones C. Investigation of the impact response of a CFRP wingbox under load for impact energies above the damage threshold. 42nd AIAA/ASCE/AHS/ASC Structures, Structural Dynamics, and Materials Conference and Exhibit, 16–19 April 2001, Seattle, Washington, USA.